

Radiation Spectrum of the Photospheric Emission for a Turbulent Relativistic Jet

GUO-YU LI,¹ DA-BIN LIN,¹ ZHI-LIN CHEN,¹ AND EN-WEI LIANG¹

¹*Guangxi Key Laboratory for Relativistic Astrophysics, School of Physical Science and Technology, Guangxi University, Nanning 530004, China*

ABSTRACT

The prompt γ -rays of gamma-ray bursts (GRBs) may originate from the photosphere of a relativistic jet. However, only a few GRBs have been observed with evident blackbody-like emission, for example, GRB 090902B. It has been demonstrated that internal dissipation processes, such as magnetic reconnection, can occur within the relativistic jet and thereby drive violent turbulence in the dissipation region. In this paper, we study the photospheric emission of a jet with turbulence below its photosphere. Here, the turbulence is modeled phenomenologically under the assumption that the four-velocity of its eddies follows a Gaussian distribution in the jet's co-moving frame. It is found that the turbulence scatters photons to high energies and thus intensifies the emission in the high-energy regime. The corresponding distortion of the radiation field can be preserved if and only if the turbulence occurs in a region with incomplete photon-electron coupling. Consequently, the observed radiation spectrum can be reshaped into a Band-like spectrum.

Keywords: Gamma-ray bursts (629): general - turbulence - magnetic reconnection

1. INTRODUCTION

Gamma-ray bursts (GRBs), first detected serendipitously in the late 1960s (Klebesadel et al. 1973), represent the most luminous electromagnetic explosions in the Universe (Kumar & Zhang 2015). Despite extensive observational efforts, the physical origin of GRB prompt emission remains a major unsolved problem in high-energy astrophysics. A key observational clue lies in their spectral properties: most GRB spectra are well-described by the empirical Band function (Band et al. 1993), characterized by a smoothly connected broken power-law shape with low-energy photon spectral index $\alpha \sim -0.8$, the high-energy photon spectral index $\beta \sim -2.3$, and the break energy $E_0 \sim 150$ keV (Yu et al. 2016). However, it is difficult to associate these parameters with the physical processes responsible for GRB emissions. Two principal mechanisms dominate theoretical discussions: synchrotron radiation (Meszaros et al. 1994; Daigne & Mochkovitch 1998; Lloyd & Petrosian 2000; Daigne et al. 2011; Zhang & Yan 2011) and photospheric emission (Thompson 1994; Mészáros & Rees 2000; Beloborodov 2010; Lazzati & Begelman 2010).

Synchrotron radiation plays a significant role in shaping GRB spectra (Zhang 2020) but faces a critical chal-

lenge in its predicted low-energy spectral index. The typical dissipation processes in the jets of GRBs usually predict that the electrons are in a fast cooling state, leading to synchrotron emission with a low-energy photon spectral index $\alpha = -1.5$ (Sari et al. 1998; Ghisellini et al. 2000). The low-energy photon spectral index predicted for synchrotron radiation is softer than observations of typical GRBs. Moreover, some GRBs have been observed to exhibit $\alpha > -1/3$, which is beyond the “death-line” of synchrotron radiation (Yang & Zhang 2018). In contrast, the photospheric emission model successfully explains certain observational correlations, such as the Amati relation and spectral peak-energy evolution (Lazzati et al. 2013; López-Cámara et al. 2014; Ito et al. 2019). However, its predicted spectrum is narrower than those of typical GRBs. In the Rayleigh-Jeans regime, pure blackbody emission is predicted to be with $\alpha \sim +1$, but relativistic and geometric effects can soften the radiation spectrum to $\alpha \sim +0.4$ (Beloborodov 2010; Deng & Zhang 2014). Although narrow spectra have been observed in some GRBs like GRB 090902B (Ryde et al. 2010; Zhang et al. 2011) and GRB 220426A (Deng et al. 2022; Wang et al. 2022), most GRBs lack such signatures.

If dissipation occurs below the photosphere, sub-photospheric electrons are heated through dissipation processes, and Comptonization of photons affects the spectrum shape (Rees & Mészáros 2005; Pe’er et al.

arXiv:2507.15242v1 [astro-ph.HE] 21 Jul 2025

2006). Simulations suggest that sub-photospheric dissipation can lead to a non-thermal radiation spectrum (Ryde et al. 2011). Various dissipation mechanisms have been considered, including magnetic reconnection (Giannios & Spruit 2005), internal shocks (Rees & Mészáros 2005), and collisional heating (Beloborodov 2010; Vurm et al. 2011). Additionally, geometric effects can broaden the photospheric emission spectrum (Pe’er 2008; Deng & Zhang 2014; Meng et al. 2018). Despite extensive studies, it remains challenging to obtain spectra with $\alpha \sim -0.8$ for the photospheric emission (Zhang 2019). We note that any dissipation mechanism in the jet inevitably drives turbulence. This turbulence, a common yet frequently overlooked feature of relativistic jets, likely plays a key role in bridging the gap between theoretical predictions and observations.

The paper is organized as follows: Section 2 provides a detailed explanation of our numerical model and describes how we incorporate isotropic turbulence and magnetic reconnection. Section 3 presents simulation results for the photospheric emission of a turbulent jet. Section 4 summarizes our results.

2. MODEL

2.1. The MCRaT Code

We use the Monte Carlo Radiation Transfer (MCRaT) code (Lazzati 2016; Parsotan & Lazzati 2018; Parsotan et al. 2018, 2020) to simulate photon propagation and scatter in a turbulent jet. In the MCRaT code, photons are injected within a radius range of $[R_{\text{inj}} - \Delta R, R_{\text{inj}} + \Delta R]$. In this paper, $\Delta R = R/(2\Gamma_b)$ is set, where Γ_b is the bulk Lorentz factor of the jet fluid and R represents the jet radius measured relative to the central engine of the burst.

The expected number of photons in the i -th fluid element is given by

$$dN_i = \frac{\zeta T_i'^3 \Gamma_i}{\omega} dV_i, \quad (1)$$

where the prime represents the parameters estimated in the co-moving frame of the jet, T_i' is the temperature of the fluid element in a co-moving frame, ζ is the number density coefficient ($\zeta = 20.29$ for a Planck spectrum, $\zeta = 8.44$ for a Wien spectrum), Γ_i is the Lorentz factor of the fluid element, dV_i is the volume of the fluid element, and ω is the weight factor of the injected photons. The code dynamically adjusts the photon weight factor ω to match the predefined total number of photons in the injection region. Each injected photon is assigned an azimuth angle $\phi' \in [0, 2\pi]$ and a polar angle $\theta' \in [0, \pi]$, where ϕ' is randomly sampled from $[0, 2\pi]$ and $\cos \theta'$ is randomly sampled from $[-1, 1]$. The four-momentum

of the i -th injected photon in the co-moving frame is defined as

$$p_i' = \frac{h\nu_i'}{c} (1; \sin \theta_i' \cos \phi_i'; \sin \theta_i' \sin \phi_i'; \cos \theta_i'), \quad (2)$$

where ν_i' is the frequency of the injected photons in the jet co-moving frame and h is the Planck constant.

Based on the density ρ_i of the fluid element encompassing the i -th photon, one can obtain the mean free path for the corresponding photon (Abramowicz et al. 1991), i.e.,

$$\lambda_i = \frac{m_p}{\rho_i \sigma_T (1 - \beta_i \cos \theta_{\text{fp},i})}, \quad (3)$$

where σ_T is the Thomson scattering cross-section, m_p is the proton mass, β_i denotes the fluid velocity (in units of c), and $\theta_{\text{fp},i}$ represents the angle between the fluid velocity vector and photon momentum. Statistically, the scattering path length l for a photon obeys the distribution of $f(l/\lambda_i) = e^{-l/\lambda_i}$. Consequently, the scattering path length for the i -th photon in MCRaT code is sampled as

$$l_i = -\frac{m_p}{\rho_i \sigma_T (1 - \beta_i \cos \theta_{\text{fp},i})} \ln \xi, \quad (4)$$

where ξ is a random number uniformly selected from $[0, 1]$. The scattering time is thus $t_{s,i} = l_i/c$. The photon with the smallest $t_{s,i}$ is assumed to scatter first, and thus the positions of all the photons are advanced by the time of $t_{s,\text{min}} = \min\{t_{s,i}\}$. Although the photon with the smallest $t_{s,i}$ is the photon of interest to scatter, the scattering is determined by the Klein-Nishina cross-section (σ_{KN}) (Mathews 2013), i.e., if $\xi < \sigma_{\text{KN}}/\sigma_T$, the photon scatters, updating its momentum and position; otherwise, only its position is updated. Here, ξ is a random number uniformly selected from $[0, 1]$. For more details on the MCRaT code, please refer to these articles, e.g., Lazzati (2016); Parsotan & Lazzati (2018); Parsotan et al. (2018, 2020).

2.2. Prescription of a Relativistic Jet

Bulk motion of the jet We employ numerical modeling to determine the fluid properties of the jet, including the bulk Lorentz factor (Γ_b), the co-moving temperature (T'), and the co-moving density (ρ'). The bulk Lorentz factor is related to the radius R of the fluid with respect to the central engine, i.e.,

$$\Gamma_b(R) = \begin{cases} R/R_0, & R \leq R_s \\ \eta, & R > R_s \end{cases}, \quad (5)$$

where R_0 is initial radius of fireball, $R_s = \eta R_0$ is the saturation radius, and η is the dimensionless entropy of

the jet. The co-moving temperature is given by

$$T'_b(R) = \frac{T_0}{2\Gamma_b(R)} \times \begin{cases} 1, & R \leq R_s \\ (R/R_s)^{-\frac{2}{3}}, & R > R_s \end{cases}, \quad (6)$$

where $T_0 = [L_j/(4\pi R_0^2 a c)]^{1/4}$ is the initial temperature for the fireball, a is the radiation density constant, and L_j is the jet's power. The co-moving density is expressed as

$$\rho' = L_j/(4\pi R^2 c^3 \eta \Gamma_b). \quad (7)$$

Turbulent motion of the fluid elements In addition to bulk motion described previously, turbulent motion also acts upon individual fluid elements. Turbulence in astrophysical jets may be powered by diverse physical mechanisms. Given the complexity of its origin, we employ a phenomenological approach to model turbulent properties. Our phenomenological model assumes isotropic turbulence in the co-moving frame of the jet, consistent with the results in numerical simulations which show a Gaussian distribution of the turbulent velocity approximately (Yamamoto & Kambe 1991; Endeve et al. 2012). Accordingly, we model the probability density functions for the three spatial components (x', y', z') of the four-velocity field as Gaussian distributions.

Owing to the expansion of the jet, we define a series of turbulent cells in the co-moving frame of the jet. Each turbulent cell has a characteristic scale of $\lambda' = R/(\chi \Gamma_b)$, where χ is a scale factor. The corresponding active timescale for eddies is $\Delta t_{\text{turb}} = \lambda'/c$. We assume that turbulent eddies are uniformly distributed in space, with a probability p to exhibit turbulent activity for any eddy. The turbulent four-velocity of the i -th turbulent cell, denoted as $\gamma'_i \beta'_{i,k} |_{k \in \{x', y', z'\}}$, is set as follows:

- if $\xi_i \leq p$, the value of $\gamma'_i \beta'_{i,k} |_{k \in \{x', y', z'\}}$ is randomly selected based on the distribution function $\mathcal{N}(0, \gamma_0'^2 \beta_0'^2)$,
- if $\xi_i > p$, $\gamma'_i \beta'_{i,k} |_{k \in \{x', y', z'\}} = 0$ is set,

where ξ_i is a number randomly selected in $[0, 1]$ and used to control the activity of the i -th cell, $\beta'_0 = \sqrt{\sigma/(1+\sigma)}$, $\gamma'_0 = (1 - \beta_0'^2)^{-1/2}$, and $\mathcal{N}(0, \gamma_0'^2 \beta_0'^2)$ is a Gaussian distribution with mean zero and variance $\gamma_0'^2 \beta_0'^2$. The value of σ is introduced to describe the intensity of turbulent motion and the value of p is used to describe the proportion of active cells. Following each Δt_{turb} interval, we resample the four-velocity components for all turbulent cells. By incorporating the bulk motion properties, i.e., Equations (5)-(7), one can obtain the overall characteristics of the turbulent jet in the lab frame of the burst.

In our phenomenological framework, different physical mechanisms driving turbulence are distinguished solely by their characteristic values of σ and p . For example, magnetic reconnection would eject high-velocity fluids and occur sporadically in space. This scenario can be described by adopting a large value of σ and a small value of p (tagged as “Type-B” in this paper). Magnetic reconnection would also drive a weak turbulent motion in the bulk region, which can be described by adopting a low value of σ and a high value of p (tagged as “Type-A”). Lazarian et al. (2019) highlights the crucial role of turbulence in enhancing reconnection efficiency in GRBs. The driven turbulence in turn triggers more magnetic reconnection, which overlies the turbulent cells of Type-A turbulence. Such turbulence is tagged as “Type-A+Type-B”. Typically, turbulence exhibits energy cascades across different scales (Schekochihin et al. 2009), of which the dynamic of turbulent eddies is similar to the Type-A+Type-B turbulence. Then, we neglected the cascade behavior of turbulence.

2.3. Basic Settings in Our Simulations

Simulation Settings In our simulations, unless otherwise specified, the fireball parameters are set as follows: $L_j = 10^{52} \text{ erg s}^{-1}$, $\eta = 100$, and $R_0 = 10^8 \text{ cm}$.² Seed photons are sampled from a Planck spectrum, and injected radius R_{inj} is set at $\tau = 30$ with optical depth $\tau(R) = L_j \sigma_T / (8\pi m_p c^3 \beta \eta^3 R)$. In addition, the photon scatter is ceased at the radius of $\tau = 0.1$. Unless otherwise specified, the turbulence in the jet is set in the region with $\tau \in [0.1, 30]$. The polar angle of the injection region is constrained to $\theta \leq 3^\circ$, where $\theta = 0$ is set at the axis of the jet. The total number of injected seed photons exceeds 10^5 . The scale factor χ for the turbulence cell is set to 10.

Observations Production To generate mock observational data, we use ProcessMCRaT code (Lazzati 2016; Parsotan & Lazzati 2018; Parsotan et al. 2018, 2020). The observer is positioned at a distance of $5 \times 10^{14} \text{ cm}$ from the central engine, with 1° deviation from the jet axis as the viewing angle, and accept photons within 3° range along the light of sight³. Due to the Doppler

² The parameters of L_j , η , and R_0 determine the temperature of the jet at the injection radius and thus affect the injected photons' energy. In simulations with different values of L_j , η , and R_0 , the radiation spectrum may be shifted globally, and thus the turbulence-induced effects on the radiation spectrum of the photosphere remain unaffected. Then, a jet with $L_j = 10^{52} \text{ erg s}^{-1}$, $\eta = 100$, and $R_0 = 10^8 \text{ cm}$ is adopted as an example.

³ In our model, the jet is unstructured with properties uniform in polar angle, and the turbulence statistics are isotropic. Then, the observed emission is not affected by the choice of viewing

shift and the geometric effect, the observed photospheric emission should be described by a multi-color blackbody (Pe'er 2008). Specifically, the multi-color blackbody emission with a cutoff power-law distribution temperature (CPL-mBB, Deng et al. 2022), i.e., $\hat{f}(T) \propto (T/T_c)^q \exp[-(T/T_c)^s]$, can well describe the photospheric emission. Based on the MCRaT for a photosphere free of turbulence, the obtained radiation spectrum can be well described by a CPL-mBB with $q = 2.8$ and $s = 0.9$ ⁴. The CPL-mBB spectrum model is used to fit the radiation spectra obtained in this paper.

3. RESULT

3.1. Spectral Broadening and High-energy Photon Formation

We first study the impact of turbulent motion intensity σ on the photospheric emission under Type-A turbulence with fixed $p = 1$. Figure 1 shows the radiation spectra of the turbulent photosphere with different values of σ . One can find that the radiation spectra are shifted to the high-energy regime by increasing the value of σ . This aligns with theoretical predictions that turbulence accelerates photons to higher energies via random scattering (Murase et al. 2012). We fit the spectra using the CPL-mBB model with $q = 2.8$ and $s = 0.9$ and the results are indicated by black dashed lines in this figure. It is notable that the radiation spectra for the cases with $\sigma = 0.01$ or $\sigma = 0.04$ are broader than the non-dissipative photospheric spectrum (i.e., the CPL-mBB model with $q = 2.8$ and $s = 0.9$). However, the radiation spectra for the cases with very high σ , e.g., $\sigma = 0.08$, exhibit only a shift, with no change in spectral morphology. The reason for this behavior will be discussed in detail in Section 3.2. Based on the fitting results with the CPL-mBB, the spectral peak energy E_p in the ν - F_ν radiation spectrum for different values of σ is plotted in Figure 2. The relation of E_p - σ can be described with a broken power law, where $E_p \propto \sigma^{2.3}$ for $\sigma < 0.1$ and $E_p \propto \sigma^{0.7}$ for $\sigma > 0.1$.

angle and angular acceptance if the viewing angle is set along the direction of jet flow. If the viewing angle is beyond the direction of the jet flow, the observed emission may be different, e.g., the flux would be very low. The main focus of this work is the effect of turbulence on the radiation spectrum, and thus the situation by setting the viewing angle beyond the direction of the jet flow is not studied.

⁴ Based on the numeric calculations, Deng et al. (2022) finds a CPL-mBB with $q = 3$ and $s = 1.2$ can well describe the photospheric emission. Such a radiation spectrum is narrower compared to the CPL-mBB with $q = 2.8$ and $s = 0.9$. This is due to the fact that photon scattering is set to cease at the radius of $\tau = 1$ in Deng et al. (2022).

We overlaid cells of magnetic reconnection on a weak turbulent bulk region, i.e., Type-A+Type-B turbulence. For Type-A turbulence, we adopt $(\sigma, p) = (\sigma_a, p_a) = (0.005, 1)$; while for Type-B turbulence, we set $(\sigma, p) = (\sigma_b, p_b)$ with $\sigma_b = 5$ and p_b varying as specified. Figure 3 presents radiation spectra for Type-A+Type-B turbulence at different values of p_b . It can be found that the high-energy regime is progressively intensified by increasing p_b . This result reveals that Type-B turbulence generates an additional component in the high-energy regime. Moreover, this component is intensified by increasing p_b . Based on the case with $p_b = 0.02$, one can find that the additional component peaks at $E_2 \sim 10^3$ keV, which is distinct from the low-energy component peaking at $E_1 \sim 20$ keV. Figure 4 shows the dependence of the flux ratio $F_\nu(E_2)/F_\nu(E_1)$ on the value of p_b . The relation follows a broken power law: $F_\nu(E_2)/F_\nu(E_1) \propto p_b^{1.2}$ for $p_b < 10^{-1.8}$ and $\propto p_b^{2.5}$ for $p_b > 10^{-1.8}$. It is worth pointing out that the value of $F_\nu(E_2)/F_\nu(E_1)$ directly affects the spectral morphology of the photospheric emission. For example, the photon spectral index α_{12} in the energy range of $E \in [E_1, E_2]$ can be estimated with $\alpha_{12} \sim \log[F_\nu(E_2)/F_\nu(E_1)]/\log[E_2/E_1]$. For the case with $p_b = 0.01$, one can obtain $F_\nu(E_2)/F_\nu(E_1) \sim 1$ and thus $\alpha_{12} \sim 0$. As shown in Figure 5, the radiation spectrum for $p_b = 0.01$ can be decomposed into three segments: $N(E) \propto E^{0.3}$ for $E \in [0.1, 2]$ keV (green data points), E^{-1} for $E \in [20, 1000]$ keV (orange data points), and $E^{-2.1}$ for $E \in [4000, 70000]$ keV (red data points). This is consistent with our above analysis. The morphology of the middle segment (i.e., the orange data points) matches the low-energy regime of typical GRB spectra, and the high-energy segment (i.e., the red data points) resembles the high-energy regime of typical GRB spectra.

3.2. Turbulent Region Effect

The appearance of the high-energy peak component arises from incomplete thermalization of photons, which are scattered by turbulence. Since the thermalization of photons is related to the optical depth τ , we study the photospheric emission by setting turbulence in different regions, as shown in Figure 6. Here, we configure Type-A+Type-B turbulence with $(\sigma_a, p_a) = (0.005, 1)$ and $(\sigma_b, p_b) = (5.0, 0.01)$. Turbulence is implemented in the region across three optical depth ranges: $\tau \in [25, 30]$ (green), $[10, 15]$ (orange), and $[1, 5]$ (red). For comparison, we also plot turbulence-free photospheric emission (blue points). One can find that the high-energy regime is intensified for a turbulent photosphere. Furthermore, such intensification weakens as the turbulent

region shifts to the inner region of the jet (corresponding to increasing τ). Since the thermalization of the photons is strengthened as τ increases, the distinct spectral signatures in the high-energy regime reflect varying degrees of thermalization efficiency. Notably, when turbulence is implemented in the $\tau \in [1, 5]$ region (red points), a shoulder emerges in the high-energy regime of the spectrum. This radiation spectrum profile resembles that of GRB 171205A's prompt emission.

Pe'er (2008) shows that the co-moving photon energy of a coasting jet decreases with radius as $\propto R^{-2/3}$, owing to the slight misalignment of the scattering electrons' velocity vectors. Moreover, this mechanism dominates photon cooling. We thus unfold electron thermalization effects by simulating a coasting jet with $T'_b \propto R^{-2}$ for its electrons' temperature. Results are shown in Figure 7, where seed photons (with initial photon temperature set to 50 times the local electron temperature) are injected at the radius of 10^{10} cm. The evolution of average photon energy $\bar{\epsilon}$ versus radius R is plotted as a blue solid line, while $k_B T_b$ versus R appears as a black solid line, where k_B is the Boltzmann constant. The strength of thermalization can be inferred by comparing the $\bar{\epsilon}$ - R and $k_B T_b$ - R relations. Strong photon thermalization is inferred if the $\bar{\epsilon}$ - R curve matches the $k_B T_b$ - R curve, while weak thermalization is indicated if deviations between the two curves occur. Figure 7 reveals strong thermalization at the injection radius, establishing thermal equilibrium between photons and electrons. As the jet expands, the thermalization weakens and the co-moving photon energy follows $\bar{\epsilon} \propto R^{-2/3}$, consistent with the theoretical expectation reported in Pe'er (2008). Notably, an extensive region below the photosphere exhibits weak thermalization of photons by electrons.

3.3. Reconcile with Band Function

Most Fermi GRBs exhibit prompt emission spectra well described by a Band function with characteristic parameters $\alpha \sim -0.8$, $\beta \sim -2.3$, and $E_0 \sim 150$ keV. In this section, we present two realizations of the turbulent photosphere model, whose emission is reconciled with the majority of Fermi GRBs.

As shown in Figures 1, 3, and 6, thermal characteristics persist in the low-energy regime. To reconcile the model with Fermi GRB observations, the spectral peak of a turbulence-free fireball must be below the *Fermi*-GBM detection threshold (i.e., 8 keV). The spectral peak of the fireball is related to the observed temperature of the photosphere, i.e., $T_{\text{ph}} = (T_0/2)(R_{\text{ph}}/R_s)^{-2/3}$, where $R_{\text{ph}} = L_j \sigma_T / (8\pi m_p c^3 \beta \eta^3) \approx L_j \sigma_T / (8\pi m_p c^3 \eta^3)$ and $\beta = \sqrt{1 - 1/\Gamma_b^2}$. The ν - νF_ν spectral peak photon energy is around $\xi k_B T_{\text{ph}} \approx 24.7 \text{ keV } \eta_2^{8/3} L_{j,52}^{-5/12}$ with

$\xi = 9.3$ based on MCRaT simulations. Then, we take a jet with $\eta = 50$ and $L_j = 10^{52} \text{ erg s}^{-1}$ as an example.

Figure 8(a) shows photospheric emission with Type-A turbulence implemented at $\tau < 30$, with parameters $\sigma = 0.04$ and $p = 0.45$. The modeled turbulence produces a Band-like spectrum in the energy range of [8 keV, 40 MeV], with spectral parameters $\alpha = -1.0$, $\beta = -3.0$, and $E_0 = 257.7 \text{ keV}$. Figure 8(b) shows photospheric emission with Type-B turbulence implemented in the region $10 < \tau < 15$, using parameters $\sigma = 7$ and $p = 0.05$. The scattered photons together with the thermal emission produce two segments of the radiation spectrum. The Band function fit to the *Fermi*-GBM's characteristic energy range yields $\alpha = -1.0$, $\beta = -2.3$, and $E_0 = 856.9 \text{ keV}$. Although the elevated E_0 exceeds typical values, such high-energy peaks are occasionally observed in exceptional GRBs. Figure 8 demonstrates that the turbulent photospheres can reproduce both typical and extreme GRB spectral features.

4. CONCLUSIONS AND DISCUSSION

This paper is focused on the effect of turbulence on the radiation spectrum of the photospheric emission. Our simulations based on the MCRaT code demonstrate that the turbulence below the photosphere plays a significant role in shaping the photospheric emission. The effect of the turbulence on the photospheric emission critically depends on the spatial distribution and velocity of turbulent eddies. If the turbulence is well developed under the photosphere of a jet, low-velocity turbulence can significantly intensify the photospheric emission in the high-energy regime by scattering soft photons to high-energies. A spectral bump may appear in the high-energy regime. Its peak photon energy increases with turbulent velocity, while its flux density F_ν rises with increasing spatial occupancy ratio of eddies.

The weak coupling between photons and electrons is required in order to preserve the distortion of the radiation field by the turbulence. We find that a wide region below the photosphere appears to exhibit weak coupling between electrons and photons. If the proportion of neutrons in the jet is significant, electrons and photons decouple more easily (e.g., Walker et al. 2024). We also demonstrate that the observed radiation spectra of *Fermi*-GBM on GRBs can be reproduced if a turbulent fireball with $k_B T_{\text{ph}} \lesssim 1 \text{ keV}$ is adopted, where T_{ph} is the observed temperature of its photosphere. If the contribution of synchrotron radiation from electrons is considered, e.g., Parsotan & Lazzati (2021), the $k_B T_{\text{ph}} \lesssim 1 \text{ keV}$ requirement for the turbulent fireball can be relaxed.

ACKNOWLEDGMENTS

We acknowledge Dr. Parsotan for the publicly available MCRaT code. We thank the anonymous referee of this work for useful comments and suggestions that improved the paper. This work is supported by the National Natural Science Foundation of China (grant Nos. 12273005, 12494575, and 12133003), the National Key R&D Program of China (grant No. 2023YFE0117200 and 2024YFA1611700), the special funding for Guangxi

Bagui Youth Scholars, and the Guangxi Talent Program (“Highland of Innovation Talents”).

Software: MCRaT (Lazzati (2016); Parsotan & Lazzati (2018); Parsotan et al. (2018, 2020)), ProcessM-CRaT (Lazzati 2016; Parsotan & Lazzati 2018; Parsotan et al. 2018, 2020), matplotlib (Hunter 2007), numpy (Harris et al. 2020).

REFERENCES

- Abramowicz, M. A., Novikov, I. D., & Paczynski, B. 1991, *ApJ*, 369, 175, doi: [10.1086/169748](https://doi.org/10.1086/169748)
- Band, D., Matteson, J., Ford, L., et al. 1993, *ApJ*, 413, 281, doi: [10.1086/172995](https://doi.org/10.1086/172995)
- Beloborodov, A. M. 2010, *MNRAS*, 407, 1033, doi: [10.1111/j.1365-2966.2010.16770.x](https://doi.org/10.1111/j.1365-2966.2010.16770.x)
- Daigne, F., Bošnjak, Ž., & Dubus, G. 2011, *A&A*, 526, A110, doi: [10.1051/0004-6361/201015457](https://doi.org/10.1051/0004-6361/201015457)
- Daigne, F., & Mochkovitch, R. 1998, *MNRAS*, 296, 275, doi: [10.1046/j.1365-8711.1998.01305.x](https://doi.org/10.1046/j.1365-8711.1998.01305.x)
- Deng, L.-T., Lin, D.-B., Zhou, L., et al. 2022, *ApJL*, 934, L22, doi: [10.3847/2041-8213/ac8169](https://doi.org/10.3847/2041-8213/ac8169)
- Deng, W., & Zhang, B. 2014, *ApJ*, 785, 112, doi: [10.1088/0004-637X/785/2/112](https://doi.org/10.1088/0004-637X/785/2/112)
- Endeve, E., Cardall, C. Y., Budiardja, R. D., et al. 2012, *ApJ*, 751, 26, doi: [10.1088/0004-637X/751/1/26](https://doi.org/10.1088/0004-637X/751/1/26)
- Ghisellini, G., Celotti, A., & Lazzati, D. 2000, *MNRAS*, 313, L1, doi: [10.1046/j.1365-8711.2000.03354.x](https://doi.org/10.1046/j.1365-8711.2000.03354.x)
- Giannios, D., & Spruit, H. C. 2005, *A&A*, 430, 1, doi: [10.1051/0004-6361:20047033](https://doi.org/10.1051/0004-6361:20047033)
- Harris, C. R., Millman, K. J., van der Walt, S. J., et al. 2020, *Nature*, 585, 357, doi: [10.1038/s41586-020-2649-2](https://doi.org/10.1038/s41586-020-2649-2)
- Hunter, J. D. 2007, *Computing in Science & Engineering*, 9, 90, doi: [10.1109/MCSE.2007.55](https://doi.org/10.1109/MCSE.2007.55)
- Ito, H., Matsumoto, J., Nagataki, S., et al. 2019, *Nature Communications*, 10, 1504, doi: [10.1038/s41467-019-09281-z](https://doi.org/10.1038/s41467-019-09281-z)
- Klebesadel, R. W., Strong, I. B., & Olson, R. A. 1973, *ApJL*, 182, L85, doi: [10.1086/181225](https://doi.org/10.1086/181225)
- Kumar, P., & Zhang, B. 2015, *PhR*, 561, 1, doi: [10.1016/j.physrep.2014.09.008](https://doi.org/10.1016/j.physrep.2014.09.008)
- Lazarian, A., Zhang, B., & Xu, S. 2019, *ApJ*, 882, 184, doi: [10.3847/1538-4357/ab2b38](https://doi.org/10.3847/1538-4357/ab2b38)
- Lazzati, D. 2016, *ApJ*, 829, 76, doi: [10.3847/0004-637X/829/2/76](https://doi.org/10.3847/0004-637X/829/2/76)
- Lazzati, D., & Begelman, M. C. 2010, *ApJ*, 725, 1137, doi: [10.1088/0004-637X/725/1/1137](https://doi.org/10.1088/0004-637X/725/1/1137)
- Lazzati, D., Morsony, B. J., Margutti, R., & Begelman, M. C. 2013, *ApJ*, 765, 103, doi: [10.1088/0004-637X/765/2/103](https://doi.org/10.1088/0004-637X/765/2/103)
- Lloyd, N. M., & Petrosian, V. 2000, *ApJ*, 543, 722, doi: [10.1086/317125](https://doi.org/10.1086/317125)
- López-Cámara, D., Morsony, B. J., & Lazzati, D. 2014, *MNRAS*, 442, 2202, doi: [10.1093/mnras/stu1016](https://doi.org/10.1093/mnras/stu1016)
- Mathews, K. 2013, *Nuclear Science and Engineering*, 173, 207, doi: [10.13182/NSE11-57](https://doi.org/10.13182/NSE11-57)
- Meng, Y.-Z., Geng, J.-J., Zhang, B.-B., et al. 2018, *ApJ*, 860, 72, doi: [10.3847/1538-4357/aac2d9](https://doi.org/10.3847/1538-4357/aac2d9)
- Mészáros, P., & Rees, M. J. 2000, *ApJ*, 530, 292, doi: [10.1086/308371](https://doi.org/10.1086/308371)
- Mészáros, P., Rees, M. J., & Papathanassiou, H. 1994, *ApJ*, 432, 181, doi: [10.1086/174559](https://doi.org/10.1086/174559)
- Murase, K., Asano, K., Terasawa, T., & Mészáros, P. 2012, *ApJ*, 746, 164, doi: [10.1088/0004-637X/746/2/164](https://doi.org/10.1088/0004-637X/746/2/164)
- Parsotan, T., & Lazzati, D. 2018, *ApJ*, 853, 8, doi: [10.3847/1538-4357/aaa087](https://doi.org/10.3847/1538-4357/aaa087)
- . 2021, *ApJ*, 922, 257, doi: [10.3847/1538-4357/ac2428](https://doi.org/10.3847/1538-4357/ac2428)
- Parsotan, T., López-Cámara, D., & Lazzati, D. 2018, *ApJ*, 869, 103, doi: [10.3847/1538-4357/aaed1](https://doi.org/10.3847/1538-4357/aaed1)
- . 2020, *ApJ*, 896, 139, doi: [10.3847/1538-4357/ab910f](https://doi.org/10.3847/1538-4357/ab910f)
- Pe’er, A. 2008, *ApJ*, 682, 463, doi: [10.1086/588136](https://doi.org/10.1086/588136)
- Pe’er, A., Mészáros, P., & Rees, M. J. 2006, *ApJ*, 652, 482, doi: [10.1086/507595](https://doi.org/10.1086/507595)
- Rees, M. J., & Mészáros, P. 2005, *ApJ*, 628, 847, doi: [10.1086/430818](https://doi.org/10.1086/430818)
- Ryde, F., Axelsson, M., Zhang, B. B., et al. 2010, *ApJL*, 709, L172, doi: [10.1088/2041-8205/709/2/L172](https://doi.org/10.1088/2041-8205/709/2/L172)
- Ryde, F., Pe’er, A., Nymark, T., et al. 2011, *MNRAS*, 415, 3693, doi: [10.1111/j.1365-2966.2011.18985.x](https://doi.org/10.1111/j.1365-2966.2011.18985.x)
- Sari, R., Piran, T., & Narayan, R. 1998, *ApJL*, 497, L17, doi: [10.1086/311269](https://doi.org/10.1086/311269)
- Schekochihin, A. A., Cowley, S. C., Dorland, W., et al. 2009, *ApJS*, 182, 310, doi: [10.1088/0067-0049/182/1/310](https://doi.org/10.1088/0067-0049/182/1/310)
- Thompson, C. 1994, *MNRAS*, 270, 480, doi: [10.1093/mnras/270.3.480](https://doi.org/10.1093/mnras/270.3.480)

- Vurm, I., Beloborodov, A. M., & Poutanen, J. 2011, *ApJ*, 738, 77, doi: [10.1088/0004-637X/738/1/77](https://doi.org/10.1088/0004-637X/738/1/77)
- Walker, N., Parsotan, T., & Lazzati, D. 2024, *ApJ*, 965, 8, doi: [10.3847/1538-4357/ad2dfa](https://doi.org/10.3847/1538-4357/ad2dfa)
- Wang, Y., Zheng, T.-C., & Jin, Z.-P. 2022, *ApJ*, 940, 142, doi: [10.3847/1538-4357/aca017](https://doi.org/10.3847/1538-4357/aca017)
- Yamamoto, K., & Kambe, T. 1991, *Fluid Dynamics Research*, 8, 65, doi: [10.1016/0169-5983\(91\)90031-D](https://doi.org/10.1016/0169-5983(91)90031-D)
- Yang, Y.-P., & Zhang, B. 2018, *ApJL*, 864, L16, doi: [10.3847/2041-8213/aada4f](https://doi.org/10.3847/2041-8213/aada4f)
- Yu, H.-F., Preece, R. D., Greiner, J., et al. 2016, *A&A*, 588, A135, doi: [10.1051/0004-6361/201527509](https://doi.org/10.1051/0004-6361/201527509)
- Zhang, B. 2019, *The physics of gamma-ray bursts*
- . 2020, *Nature Astronomy*, 4, 210, doi: [10.1038/s41550-020-1041-3](https://doi.org/10.1038/s41550-020-1041-3)
- Zhang, B., & Yan, H. 2011, *ApJ*, 726, 90, doi: [10.1088/0004-637X/726/2/90](https://doi.org/10.1088/0004-637X/726/2/90)
- Zhang, B.-B., Zhang, B., Liang, E.-W., et al. 2011, *ApJ*, 730, 141, doi: [10.1088/0004-637X/730/2/141](https://doi.org/10.1088/0004-637X/730/2/141)

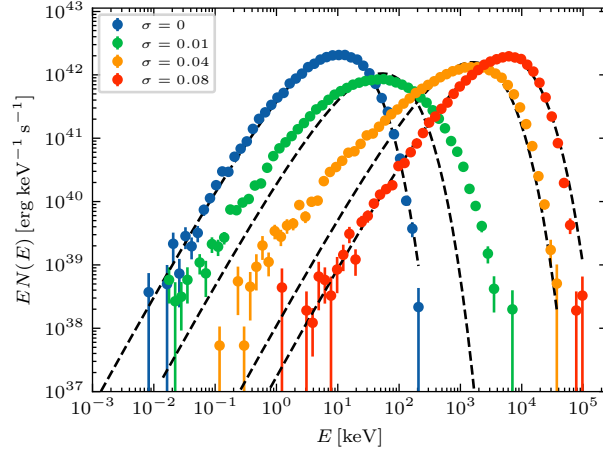


Figure 1. Radiation spectra of the Type-A turbulent photosphere for different σ values (fixed $p = 1$). Black dashed lines show the corresponding spectral fitting based on the CPL-mBB model with $s = 0.9$ and $q = 2.8$.

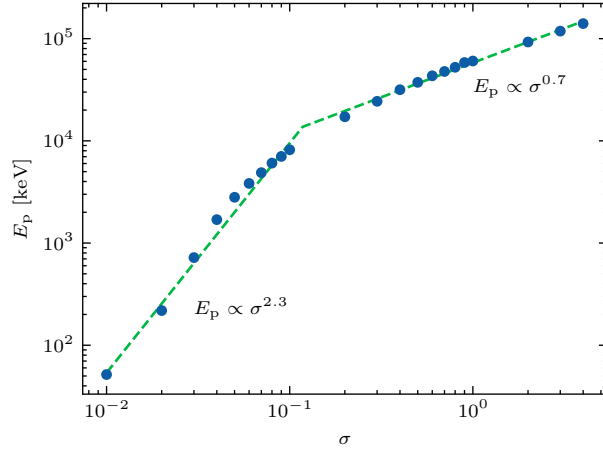


Figure 2. Dependence of E_p on σ for Type-A turbulence ($p = 1$), where the green dashed line indicates the best-fit with broken power law for E_p - σ relation.

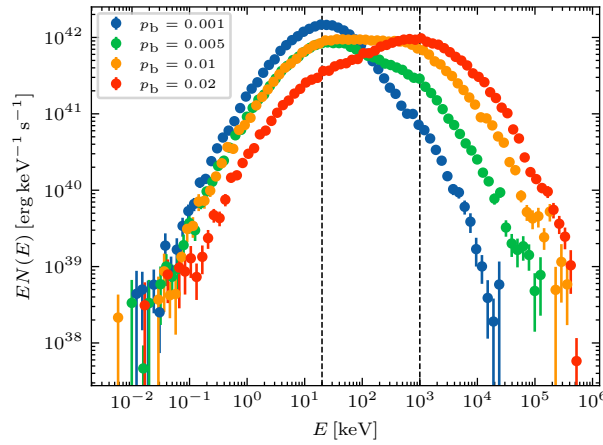


Figure 3. Radiation spectra for Type-A+Type-B turbulence by varying p_b , where $(\sigma_a, p_a) = (0.005, 1)$ and $(\sigma_b, p_b) = (5, p_b)$ are set. The left and right black dashed lines mark energies $E_1 = 20$ keV and $E_2 = 1000$ keV, respectively.

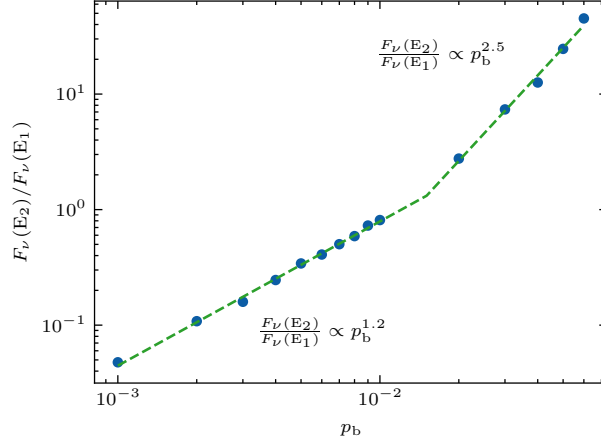


Figure 4. Dependence of the flux density ratio $F_\nu(E_2)/F_\nu(E_1)$ on p_b , with fixed $(\sigma_a, p_a) = (0.005, 1)$ and $(\sigma_b, p_b) = (5, p_b)$. The green dashed line indicates the best-fit broken power law to the $F_\nu(E_2)/F_\nu(E_1)$ - p_b relation.

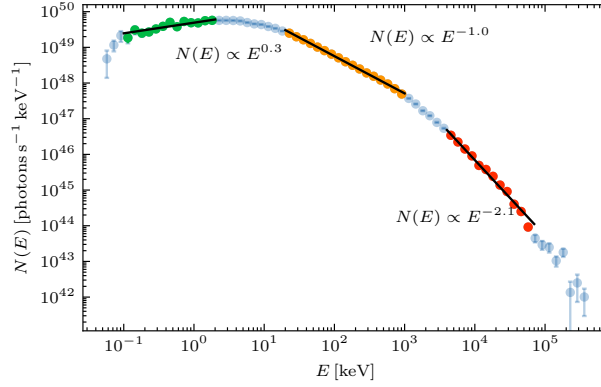


Figure 5. Photon spectrum from MCRaT simulation with $\sigma_a = 0.005$, $p_a = 1$, $\sigma_b = 5$, and $p_b = 0.01$. Black solid lines mark the best-fit power-law functions to three spectral segments: $N(E) \propto E^{0.3}$ (low-energy regime), $N(E) \propto E^{-1.0}$ (mid-energy regime), and $N(E) \propto E^{-2.1}$ (high-energy regime).

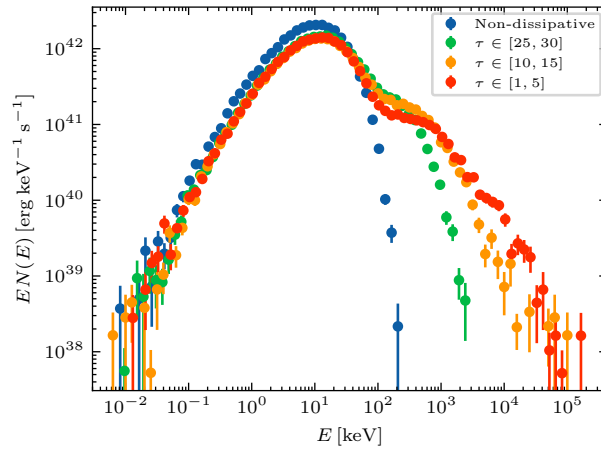


Figure 6. Photospheric emission with turbulence implemented in different regions with $\tau \in [25, 30]$ (green), $\tau \in [10, 15]$ (orange), or $\tau \in [1, 5]$ (red). Type-A+Type-B turbulence with $(\sigma_a, p_a) = (0.005, 1)$ and $(\sigma_b, p_b) = (5.0, 0.01)$ are adopted. For comparison, the photospheric emission free of turbulence is also plotted with blue points.

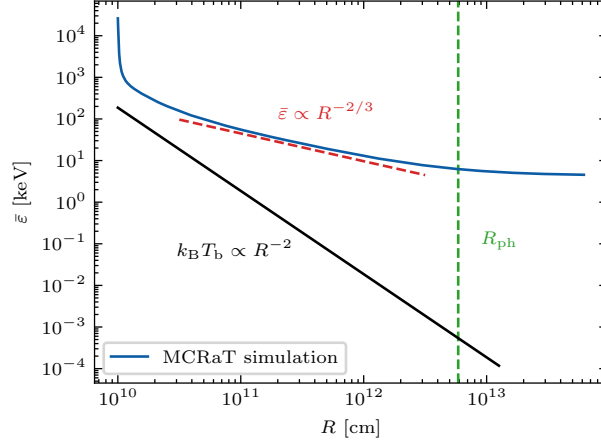


Figure 7. Demonstration of the thermalization for photons: $\bar{\varepsilon}-R$ (blue line) vs. $k_B T_b - R$ (black line), where a coasting jet with $k_B T_b \propto R^{-2}$ (black line) is adopted. The red dashed line depicts the theoretical prediction $\bar{\varepsilon} \propto R^{-2/3}$ (Pe’er 2008) and the vertical green dashed line indicates the radius of $\tau = 1$.

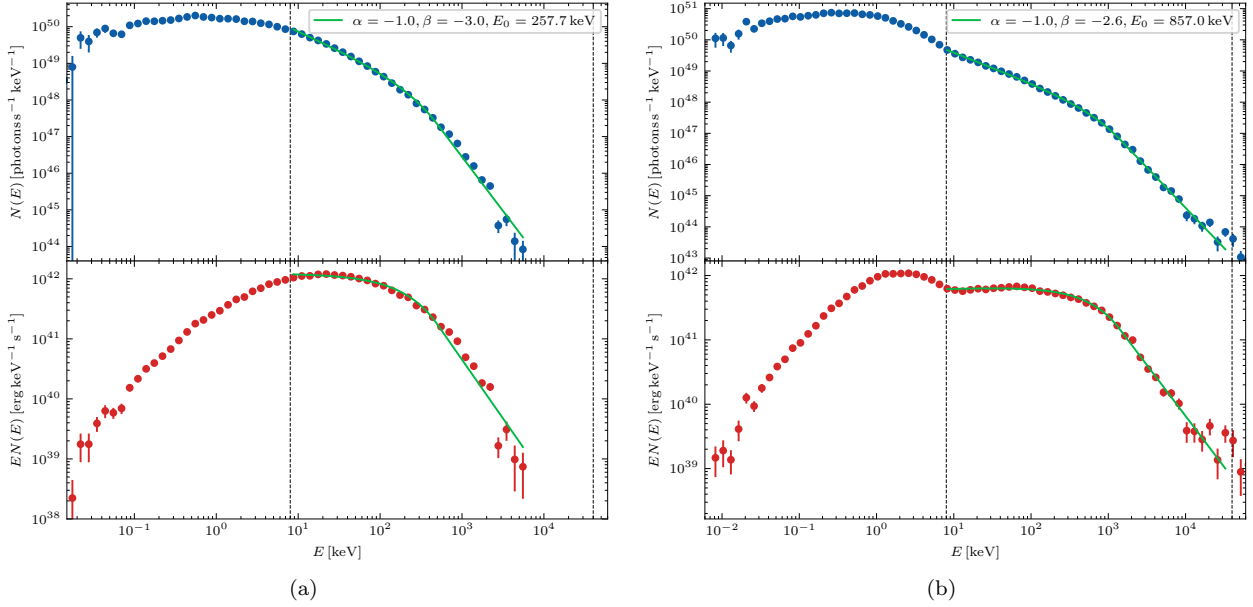


Figure 8. Demonstration of two cases to reproduce the Band-like radiation spectrum: (a) Type-A turbulence with $(\sigma, p) = (0.04, 0.45)$ and turbulence implemented in the region of $\tau \in [0.1, 30]$, (b) Type-B turbulence with $(\sigma, p) = (7, 0.05)$ and turbulence implemented in the region of $\tau \in [10, 15]$. The blue and red data points show the photon spectrum $N(E)$ and the energy spectrum $EN(E)$, respectively. The green solid line displays the best-fit Band function modeled over the *Fermi*-GBM characteristic energy range 8 keV to 40 MeV.